Impact of rutile and anatase phase on the photocatalytic decomposition of lactic acid

Annika Holm[a,b], Marwa Hamandi[b], France Simonet[b], Bernadette Jouguet[b], Frederic Dappozze[b], Chantal Guillard[b,*]

[a] Sonoma State University, CA, USA

[b] University of Lyon, Institute of Researches on Catalysis and Environment in Lyon (IRCELYON) CNRS, Université Claude Bernard Lyon 1, Villeurbanne, France

ARTICLE INFO

ABSTRACT

Rutile TiO$_2$ photocatalysts with high surface area were synthesized by hydrolysis of TiCl$_4$ in aqueous solution during 2 h and 48 h and either treated at 300 °C or not. These samples of home-made rutile TiO$_2$ were characterized by X-ray diffraction (XRD), electron microscopy (ESEM and TEM), BET surface area analysis, TG-DTA-MS and UV–vis diffuse reflectance spectroscopy. All four home-made (HM) TiO$_2$ photocatalysts are nanorods of pure rutile TiO$_2$ with surface areas between 92 and 173 m^2/g. The photocatalytic efficiencies of HM rutile samples were compared with those of commercial rutile, anatase and mixed anatase/rutile towards the degradation of lactic acid (LA), and discussed in regards to the adsorption sites. Our results showed (i) it is possible to obtain a rutile TiO$_2$ more efficient than TiO$_2$ P25 and (ii) the time of hydrolysis and calcination have an important impact on photocatalytic efficiency. The analysis of organic intermediates present in aqueous and gaseous was also performed. At similar LA conversion, high pyruvic acid selectivity was observed only in the case of the two commercial rutile TiO$_2$ samples.

1. Introduction

Titanium dioxide has been widely studied as a potential depolluting agent in the degradation of waste water and the indoor air treatment [1–4]. The interest comes from its high efficiency and availability compared to other semiconductors. TiO$_2$ is polymorphic and categorized by two main forms: anatase and rutile. Rutile TiO$_2$ is considered to be more stable than anatase, with a smaller band gap energy of 3.02 eV. Anatase TiO$_2$, with a band gap energy of 3.23 eV is considered to be more active. Actually, in the presence of most organic pollutants, anatase TiO$_2$ displays higher photocatalytic efficiency than rutile TiO$_2$. The reason for this difference remains unclear, however many hypotheses exist.

The significantly lower recombination rate of (e-, h+) pairs in presence of anatase TiO$_2$, resulting in a longer excited state lifetime is often mentioned as an influencing factor [5,6]. Luttrell's group claims it is due to a difference in band gap size, exciton mobility, as well as electron-hole pair lifetime [7]. Hirakawa's group suggests that the cause is a difference in active oxygen formation at the surface of anatase and rutile TiO$_2$ [8]. The difference could also be due to a variation in the density of surface hydroxyl groups [9], to a low adsorption capacity

of pollutant [10] or to a different capacity of O$_2$ adsorption [11–13]. A. Y. Ahmed et al [14] also showed the importance of crystal surface. It was found that rutile (001) surface exhibits ˙OH generation activity comparable to that on the anatase (101) surface whereas the other rutile crystal surfaces present a minimum OH° radical generation activity.

It has often been found that composites of anatase and rutile display the highest photocatalytic efficiency. This is true for a commercially available photocatalyst called P25 (70–80 % anatase and 20–30 % rutile). One explanation is that electron transfer can occur between the two phases, causing an increase in charge separation and a lengthening in electron-hole pair lifetime [11].

In all cases, one of the key factors in the efficiency of titanium dioxide (along with high crystallinity) is the generation of reactive oxygen species- specifically O$_2$˙-, OH˙, HO$_2$˙-, and H$_2$O$_2$. They are formed by the reactions of H$_2$O and O$_2$ with photogenerated electron-hole pairs on the surface of TiO$_2$. OH° radicals are considered the most reactive oxygen species toward organic molecules [15–17].These species act as oxidizing agents in the presence of organic molecules, leading to complete or partial mineralization [18].

Lactic acid was used as an organic pollutant model for our study. Its

---

* Corresponding author.
  E-mail address: chantal.guillard@ircelyon.univ-lyon1.fr (C. Guillard).

presence in agro-industrial and agricultural waste is significant. Agricultural byproducts present a growing threat to water and air quality. Lactic acid is also a natural product in many organisms; however, it can become toxic at high enough concentrations, especially when oxygen levels are low [19,20]. It is also a major product of fermentation, along with many other low molecular weight acids. It is also interesting due to the presence of two types of functional groups: an alcohol and carboxyl. Rather than focusing on destruction of these acids, a more desirable option is to take agricultural and industrial byproducts and transform them into desirable products for reuse. It is important to understand the transformation of these types of natural products, and if possible, derive some new desirable product from their photocatalytic degradation.

The aim of this paper is to expand our knowledge on the photocatalytic efficiency of rutile titanium dioxide by elaborating different rutile phases with high surface area, and comparing their photocatalytic efficiency in regards to other commercial rutile, anatase and mixed anatase/rutile samples. We will take into account the surface area and the adsorption properties of these different catalysts, and also the intermediate products formed in the degradation of lactic acid- it may be that the nature of the TiO_2 phase has an impact on the chemical pathways.

2. Materials and methods

2.1. Chemicals

All the materials acquired were analytical reagents and used without further purification. Lactic acid (80%), pyruvic acid (100%), acetic acid (99.7%) were supplied by Sigma Aldrich. Ultrapure water ($18 \, M\Omega.cm^{-1}$) was used throughout the whole experiments.

Seven commercial titanium dioxide were used. TiO_2 P-25 and TiO_2 P90 (80% anatase, 20% rutile) from Evonik, two TiO_2 (100% rutile) MPT-625 from ISK (Ishihara SangyoKaisha), Japon named C-R100 and C-R160 from Nanostructured and Amorphous Materials; and three anatase structure, PC105 and PC-500 titanium dioxide from Millennium, and Hombikat UV100 purchased from Sachtleben Chemie (Duisburg, Germany) and four home-made TiO_2 catalysts as describe below.

2.2. Preparation method for TiO_2

Titanium Tetrachloride (99%) was cooled to 0 °C, and maintained under continuous stirring. Distilled water was added dropwise to the precursor to generate a 3 M solution. Upon addition of water, a viscous yellow sol gel was formed, along with a large amount of chlorine gas. The 3 M solution was taken off the ice, and diluted further with distilled water at 70 °C. The new solution with a concentration of 0.3 M became almost completely transparent, and no additional gas was formed. The solution was immediately placed in a 70 °C oven where hydrolysis continued without stirring. Two methods were tested: hydrolysis in the oven for 2 h and for 48 h.

After hydrolysis, the solution turned a cloudy white color, and a precipitate began to settle at the bottom of the container. The solid was washed using centrifugation until the solution's pH was above 6. Some of the solid was lost during the washing process because of poor separation with centrifugation (even at 10,000 rpm). The remaining solid was dried in the oven at 70 °C overnight. This same washing and drying process was repeated for the 48 h hydrolysis sample. The yield varied slightly between the 2 h and 48 h samples. A portion of each catalyst was separated and calcined at 300 °C for a duration of 2 h.

The four samples differ by hydrolysis time and whether or not further heat treatment was applied (calcination vs. no calcination). The samples obtained without calcination after 2 h and 48 h of hydrolysis were named HM-R2 and HM-R48. The samples named HM-R2c and HM-R48c correspond to both previous samples calcined at 300 °C.

2.3. Characterization

Nitrogen physisorption measurements at 77 K were carried out using a Micromeritics ASAP 2020 instrument. The Brunauer-Emmett-Teller (BET) method was used to determine the specific surface areas using the adsorption data branch in the relative P/P_0 pressure range going from 0.05 to 0.25. The Barrett-Joyner-Halenda (BJH) model was used to obtain pore size distributions.

X-ray Diffraction (XRD) analyses were performed using a Bruker D8 Advance A25 diffractometer with CuK_α radiation (λ = 1.54184 Å). Crystallite sizes were obtained using the Scherrer equation (L = Kλ/$\beta cos\theta$)

where L is the crystallite size, λ is the wavelength ofX-ray radiation, β is the full width at half-maximum, and K the shape factor taken as 1.

UV-vis diffuse reflectance spectroscopy (UV–vis DRS) measurements were performed using an AvaSpec-2048 Fiber Optic Spectrometer with a symmetrical Czerny-Turner design. Spectra were recorded from 250 to 800 nm using a 2048 pixel CCD detector array. Band gap energy values were evaluated using the Kubelka–Munk method.

X-ray photoelectron spectroscopy (XPS) studies were carried out using a KRATOS Axis Ultra spectrometer equipped with a dual Al/Mg anode and a hemi-spherical analyzer operating at fixed pass energy of 40 eV A 150 W monochromatic source (Al Kα = 1486.6 eV) was used to excite the samples. The samples were pressed on an indium foil attached to the sample holder and placed into the XPS instrument. Binding energies were obtained with a precision of $\pm$ 0.2 eV.

Relative estimations of hydroxyl group presence on home-made TiO_2 rutile have been performed by the simultaneous thermogravimetric and differential thermal analyses coupled to mass spectrometer (TG-DTA-MS). TG-DTA-MS analyses were conducted on a Setaram Setsys Evolution 12 thermoanalyzer coupled via a heated (ca. 150 °C) capillary with a Pfeiffer Omnistar quadrupole mass spectrometer (QMS). For TG-DTA-MS experiments, samples (50 mg) were placed in Pt-based open crucibles and heated from ambient temperature to 900 °C, at a constant rate of 10 °C min^{-1}, under a flow of pure argon (50 Ncm^3. min^{-1}).

ICP analysis was performed by using the atomic absorption spectrometer ICP-OES ACTIVA Horiba Jobin Yvon after dissolution of the catalyst in a mixture of H_2SO_4 + HNO_3 + HF, evaporation of the solution and then solubilisation in HNO_3

A TermoFisher ESEM-QUATTRO-S was used to characterize the morphology of all home-made catalysts and two commercial rutile samples. The samples are introduced directly to the microscope without additional preparation. The experiments were run at 15 kV beam energy in the high vacuum mode, and the images were done with the Everhart-Thornley Detector (ETD).

Home-made rutile catalysts without calcination are also analyzed in a TEM (JEM2010), with LaB6 filament. This microscope is equipped with an energy diffraction analysis of X-rays (EDX). The beam energy was 200 kV

The Point of Zero Charge (PZC) of the particles, also named Isoelectric Point (IEP), was determined from the measurement of dynamic mobility thanks to a Colloidal Dynamics Zeta Compact instrument (CAD instrumentation). Suspensions were prepared by dispersing 0.05 g.L^{-1} of powder in KCl (0.1 M) and the pH was adjusted to different values between 3–8 (using either HCl for acidic pH or NaOH for basic pH). The powder was then dispersed under vigorous agitation and ultrasonic treatment for 15 min (150 W, 20 kHz) before the pH was measured. Once the suspension is loaded into the sample reservoir and pumped up through the measurement cell, the zeta potential is measured by applying a high frequency electric field across two diamond-shaped platinum-coated electrodes about 2 cm apart in the flow stream. TiO_2 particles are irradiated by a laser source and filmed by the program, allowing the determination of the dynamic mobility and the zeta potential. The isoelectric point (IEP) was then deduced from the variation in zeta potential as function of pH.

2.4. Photocatalytic experiments and analytical procedures

The photocatalytic experiments were conducted using an aqueous solution (100 cm^3) of 1000μM lactic acid (pH = 3.6). The reactions were carried out in a batch-type cylindrical photo-reactor cell made of Pyrex glass (5 cm in diameter and 250 ml volume) with mechanical stirring. It is in agreement with the standard "CEN TC 386 WI 00386020:2017". To avoid heating of the solution, water was circulated through a cylindrical jacket located around the reactor. To promote turbulence, a baffle was added to the propeller stirrers. A photograph of the reactor showing the type of stirrer used and the location of the irradiation source is given in supplementary materials (Supplementary figure S1). For all degradation experiments, 1 g L^{-1} of photocatalyst was used. This amount was determined by measurement of light transmitted with varying amounts of catalyst until less than 1% of transmitted photon flow was obtained. However, it is impossible to exclude the possibility of scattered photons. A PLL18 W Philips lamp was utilized for UV irradiation (365 nm) with irradiance power of 6 mW/cm^2 measured at the bottom of the reactor. Prior to UV irradiation, the suspensions were allowed to reach adsorption equilibrium by stirring in the dark for 1 h. Samples of the reaction solution were taken periodically during UV treatment, and filtered on a DURAPORE 0.45 μm hydrophilic membrane (Merck Millipore) before analysis. The samples were analyzed with a Shimadzu HPLC equipped with a Coregel-87H3 column (300 mm × 7.8 mm – Concise Separations) thermostated at 30 °C A H$_2$SO$_4$ (5.10^{-3} mol L^{-1}). The mobile phase was used at a flow rate of 0.7 mL min^{-1}. A Diode Array detector is set at 210 nm.

Gas was streamed into a multi-detector CP-3800 (Varian Inc) gas chromatograph by a continuous air or argon flux (50 ml.min^{-1}). CO$_2$ was analysed on a 30m*0.32mm*20 μm PLOT-Q column (Agilent technologies) by a Flame Ionisation Detector with a methanization module. Acetaldehyde was analysed on a 6m*0.32mm*0.5 μm RTx-Wax column (Restek) by a Pulsed Discharge Photoionization Detector fed with Argon-doped Helium (Ar-PDPID). Oven temperature was set at 30 °C for 10 min, then heated at 10 °C.min^{-1} up to 200 °C, and then maintained for 5 min

3. Results and discussion

3.1. Structural and morphological properties

The surface area, IEP, crystallite size and crystalline phase of the commercial catalysts are reported in Table 1. Aside form the experimentally determined IEP of PC105 and the characterization of MPT-625 and R-160, all the other characterizations come from the supplier or the literature.

The XRD patterns (Fig. 1) of the four home-made samples are similar, verifying that they are all in fact pure rutile phase. The main exposed faces are the faces 110 (100%), 101(58%), 211 (50 +/- 5%) and 111 (27–30%), which are similar to the commercial rutile samples

Structure, crystallite size, BET specific surface area, pore size, IEP, and band gap of the home made TiO$_2$ were reported in Table 2. No difference between band gap energy values was found. The Eg value of 3.00 eV corresponds to TiO$_2$ rutile. The IEP values for all commercial
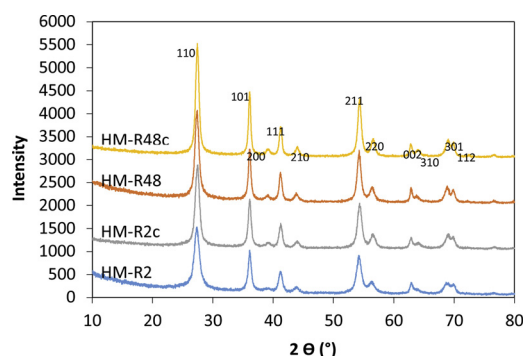

Fig. 1. XRD diffractogram of home-made TiO$_2$ materials.

TiO$_2$ samples and the two non-calcined home-made TiO$_2$ rutile samples (HM-R2 and HM-R48) were between 4.7 to 6.6. After calcination, the IEP of home-made TiO$_2$ decreased to a value of about 3.6 indicating an acidification of the surface that is unexplained (Supplementary figure S2).

The hydrolysis time and calcination influence the specific surface areas and crystallite size. Increasing the hydrolysis time leads to a decrease in surface area from 173 m^2. g^{-1} to 117 m^2. g^{-1} for non-calcined materials and from 112 to 92 m^2. g^{-1} for calcined ones. The slight increase in crystallite size of about 2–3 nm after calcination is in agreement with the decrease in surface area. The crystallite sizes obtained after calcination are similar to the crystallite size of commercial rutile MPT-625 (Table 1). BJH pore size distributions ((Supplementary figure S3) indicate a progressive shift toward higher pore diameter values after calcination. The maximum pore size distribution shifts from 21.0 nm for (HM-R2) to 26 nm for (HM-R2c). This maximum is related to the intra-particle void formed between aggregated bundles of nanoparticles. It shows that calcination tends to increase attractive Van der Waals forces, keeping TiO$_2$ nanoparticles in aggregated assemblies. Interestingly, one should also note two shoulders- the first is between 8 nm and 13 nm and the second is at 6 nm, corresponding to the porosity resulting from the nanoparticle morphology.

XPS analysis of the two commercial rutile catalysts MPT-625 and C-R160 reveals the presence of 5% Si and trace amounts of Na in the case of C-R160 and traces of Fe and Al in MPT-625 (Supplementary figure S4). The amounts of Fe and Al, measured by ICP analysis are respectively 0.2% and 2.2%.

MEB images (Fig. 2a) show that in all cases agglomerate particles are observed, and that all the catalysts are nanorods. However, the morphology of commercial rutile MPT-625 particles is irregular- there is a mixture of nanorods and spheres present. In the images of commercial rutile C-R160, nanorods are wrapped by organic impurities. These results were further confirmed by the release of organic molecules during stirring and irradiation of this materials in water.

Considering the home-made rutile catalysts, the nanorods obtained with a higher hydrolysis time are in average longer: 20–60 nm for 2 h and 40–100 nm for 48 h of hydrolysis. Regardless of the hydrolysis time, no variation in nanorod length is observed after calcination. However, after calcination at 300 °C we are able to better distinguish nanorods due to an improvement in crystallization for rutile phase.

Table 1
Structure, surface area, IEP and crystallite size of the commercial photocatalysts.

Photo-catalyst	P25	P90	PC105	PC500	Hombikat UV100	MPT-625 (C-R100)	C-R160
structure	80% Anatase 20% Rutile	80% Anatase 20% Rutile	100% Anatase	100% Anatase	100% Anatase	100% Rutile	100% Rutile
BET surface area (m^2/g)	50	90	88	340	330	103	160
Crystallite size	21-30	14	15-25	5-10	< 10	13	8-10
IEP	7 [41] -6.4 [42]	7 [41] -6.6 [42]	4.7 +/-0.5	6.2 [41]	5.3 [42]	5.4 +/-0.5	5.1 +/-0.5

Table 2
Structure, crystallite size, BET specific surface area, pore size, IEP and band gap of the home made TiO$_2$.

Photo-catalysts	Structure	S_{BET} (m^2. g^{-1})	Eg (eV)	Cristallite size (nm)	Pore volume (10^{-2} cm^2. g^{-1})	Pore size (nm)			IEP
						Type 1	Type 2	Type 3	
HM-R2	100% Rutile	173	3.0	7.5	2.2	21	13	7	4.3
HM-R2c	100% Rutile	112	3.0	9.9	0.7	26	10	6	3.5
HM-R48	100% Rutile	117	3.0	10.5	1.7	22	8	6	4.4
HM-R48c	100% Rutile	92	3.0	12.8	0.9	25	8	6	3.6
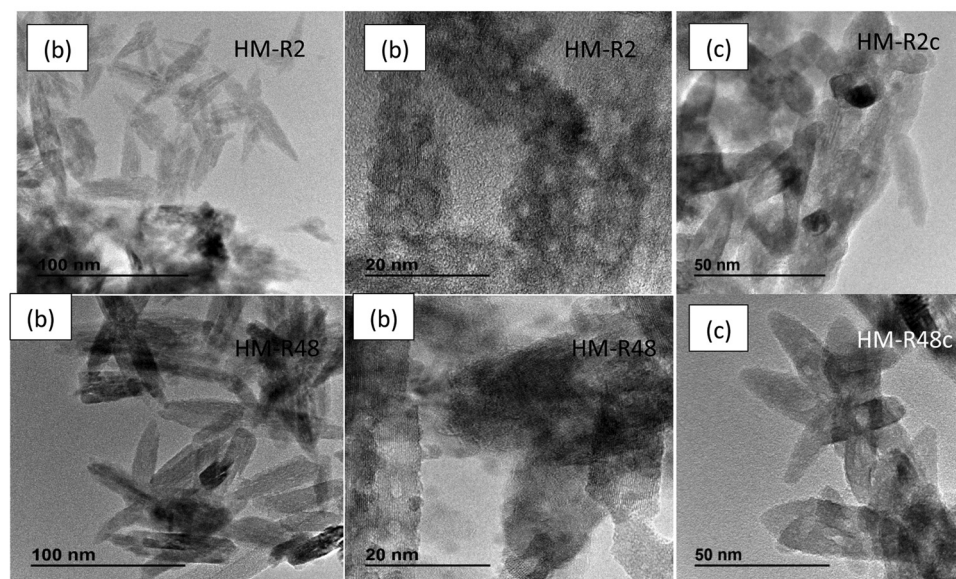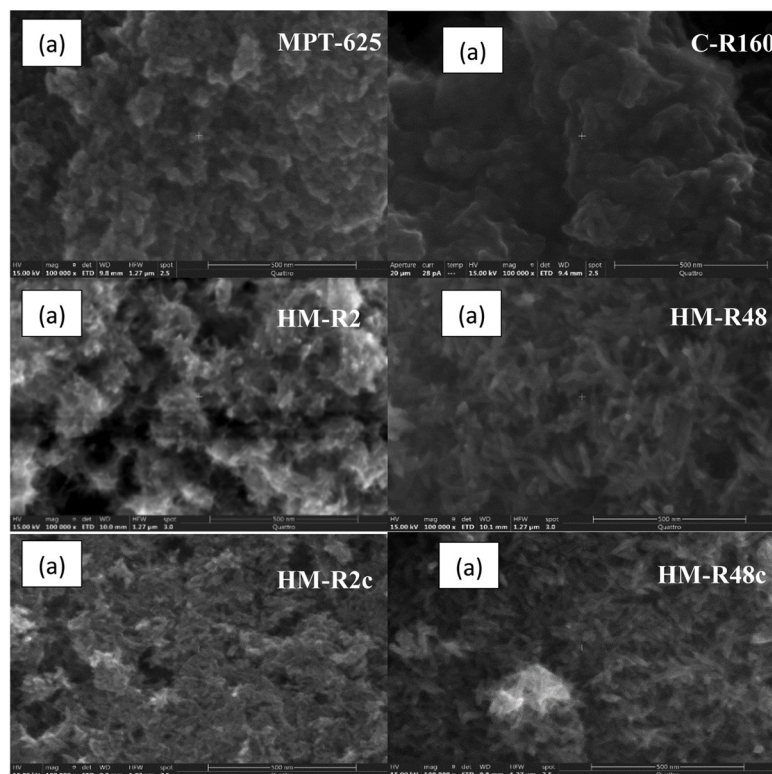
Fig. 2. (a) MEB images of commercial rutile catalysts and of the synthesized rutile catalysts after 2 h and 48 h of hydrolysis before and after calcination (scale bars correspond to 500 nm), (b) TEM images of synthesized rutile before calcination and (c) after calcination.
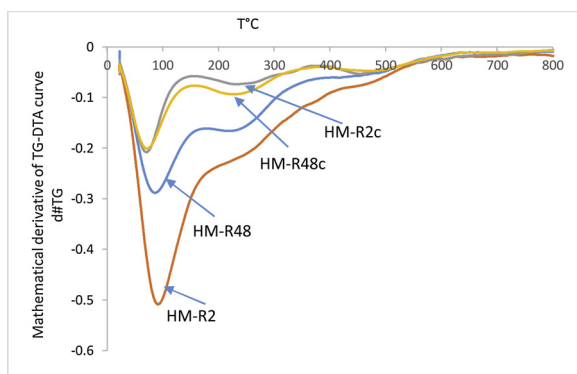
Fig. 3. Mathematical derivative of TG- DTA-MS analysis curves for the four home-made rutile TiO$_2$ samples.

The TEM images of non-calcined home-made rutile catalysts (Fig. 2b) clearly show the formation of nanorods. The enhanced images on the right also emphasize the "pores" on each individual nanorod, having a diameter of about 4 nm.

The TG-DTA-MS analysis of home-made rutile samples are given in Supplementary Figure S5a. Three weight losses were observed during the progressive heating of the samples. These weight losses are clearly observed by representing the derivative of weight losses (Fig. 3a), and are attributed to OH groups confirmed by MS analysis (Supplementary Figure S5b). The first weight loss below 160 °C corresponds to physical desorption of H$_2$O (dehydration) [21]. The weight losses in the 160–350°C and 350–600°C ranges can be related to weakly bonded OH groups and strongly bonded OH groups, respectively [22]. It is not possible to give a real value of the number of OH per nm^2 because the MS is not calibrated. However, taking into account the loss of the weight from about 160 °C–550 °C corresponding to structural OH groups, the number of OH per nm^2 is about 10α for non-calcined HM rutile samples and 5α after calcination. α is the calibration factor. Therefore, it is clear that after calcination of HM samples the amount of OH groups decrease.

4. Photocatalytic degradation of lactic acid in presence of anatase and rutile phase

4.1. Photocatalytic disappearance of lactic acid in presence of anatase, rutile and anatase/rutile TiO$_2$ samples

In order to analyze the impact of structural and textural properties, several different phases of titanium dioxide with varying surface areas were tested: three commercial pure anatase samples (PC105, PC500 and Hombikat), two commercial mixed anatase (80) / rutile (20) samples (P25 and P90), two commercial rutile (C-R100 and C-R160) and four home-made rutile samples (HM-R2; HM-R2c, HM-R48; HM-R48c)

During photocatalysis, pollutant adsorption is necessary for degradation to occur, so it is important to first determine the impact of structural/textural properties on the LA adsorption.

The amount of LA adsorbed on these different TiO$_2$ samples are represented in Fig. 4a and the amount of LA molecules adsorbed per nm^2 is reported in supplementary materials (Table S1). Considering the pH of the solution of 100 ppm LA (pH = 3.6), the pKa of LA and the IEP of all TiO$_2$ catalysts, (except for calcined home-made TiO$_2$ catalysts) the TiO2 surfaces are mainly positively charged (Ti $-$ OH$_2^+$). In the case of home-made rutile calcined TiO$_2$, at a reactional pH of 3.6, the TiO$_2$ surface charge has about an equal amount of negative charge (TiO$^-$) and positive charges (Ti(OH)$_2^+$). In other words, there is significantly more TiO$^-$ present on these calcined samples than on all other samples. In this case, the low adsorption of LA can be explained by the PZC values due to repulsion between TiO- surface and CH$_3$CHOHCOO- while

for all other TiO$_2$ samples, the TiO$_2$ surface charge cannot explain the different adsorptions of LA.

Considering Fig. 4a, it seems that LA adsorption increases as a function of the surface area, until reaching a pseudo plateau at about 30 μmol of LA. For the samples included below a surface area of 120 m^2/g, the number of LA molecules adsorbed per nm^2 is 1.1 $+/-$ 0.2. These samples include mixed anatase/rutile phases, pure anatase PC105 and pure home-made rutile samples HM-R2 and HM-R48, suggesting that the phase type has no impact on this relationship. At higher surface areas, the number of LA molecules adsorbed per nm^2 is about 0.6 $+/-$ 0.1 for Hombikat and PC500 samples (Table S1). The halved surface LA density obtained for Hombikat and PC500 could be attributed to surface OH density. The surface OH density of TiO$_2$ P25 is 5 $+/-$ 0.5 OH/nm^2, which is about twice as high as the value for TiO$_2$ Hombikat: 2.2 OH/nm^2 [23–25]. The adsorption on OH groups is in agreement with the observed adsorption of carboxylic acid on TiO$_2$ [26]. In the case of lactic acid, a bidentate adsorption involving a carboxyl group and OH group was found [27] by in situ infrared spectroscopy. In the case of calcined home-made rutile samples, the number of OH groups per nm^2 is also in agreement with the higher adsorption of LA on non-calcined home-made rutile samples (Table 2). However, in this case the low IEP values for calcined catalysts could also explain their low LA adsorption.

There are several samples that do not fit the trend- most notably C-R160, C-R100, HM-R2c and HM-R48c. Although the commercial catalysts C-R100 and C-R160 are both pure TiO$_2$ rutile phase, they also contain some other atoms in their structure. 2% of Al and traces of Fe were detected by ICP for the C-R100 sample, and 5% of Si was detected on the surface of C-R160 by XPS, along with some organic impurities highlighted during its irradiation in aqueous solution. These impurities likely block the pollutant molecule, resulting in low adsorption.

Furthermore, the thermal treatment used during the synthesis of both HM-R2c and HM-R48c can cause dehydration reactions to take place, removing some of the surface hydroxyl groups. This hypothesis is in agreement with adsorption of LA directly on the surface OH groups and could explain the low adsorption of lactic acid on calcined samples and high adsorption on non-calcined samples.

The amount of lactic acid adsorbed per nm^2 of surface (surface LA density) appears to play an important role in the efficiency of the photocatalyst (Fig. 4).

As the surface LA density increases, so does the lactic acid degradation rate- regardless of the phase type or surface area of TiO$_2$. It is generally understood that, under most circumstances, anatase/rutile and pure anatase TiO$_2$ are more efficient than pure rutile phase, [8,11,28] and that rutile phase photocatalysts generally show lower efficiency [7,29]. However, in our case, phase does not seem to be the governing factor. Indeed, two of our home-made rutile catalysts with significant surface LA density perform similarly to the high efficiency commercial composites (P25, P90).

From these results, we can conclude that the amount of organic compound adsorbed per nm^2, or the "surface organic compound density", is the deciding factor in terms of efficiency.

By comparing the degradation rates of each photocatalyst (Fig. 5), the anatase/rutile composites, the anatase phase samples of similar surface area and two rutile samples possess the highest efficiency. However, for rutile phase titanium dioxide, mixed results are gathered. There are two high performing samples, and the rest are relatively low performing. These results are in agreement with adsorption capacity and especially with surface LA density. One exception is C-R100. For this photocatalyst, the surface LA density is low; however, this sample contains a significant amount of iron. Unlike the hindrance of activity caused by impurities in C-R160, iron in C-R100 allows for photo-Fenton reactions to take place when H$_2$O$_2$ is present. It has been established that hydrogen peroxide is formed during the ROS generation process [30,31]. With more hydroxyl radicals formed, the degradation rate is likely to increase, meaning that the high efficiency could be due to the
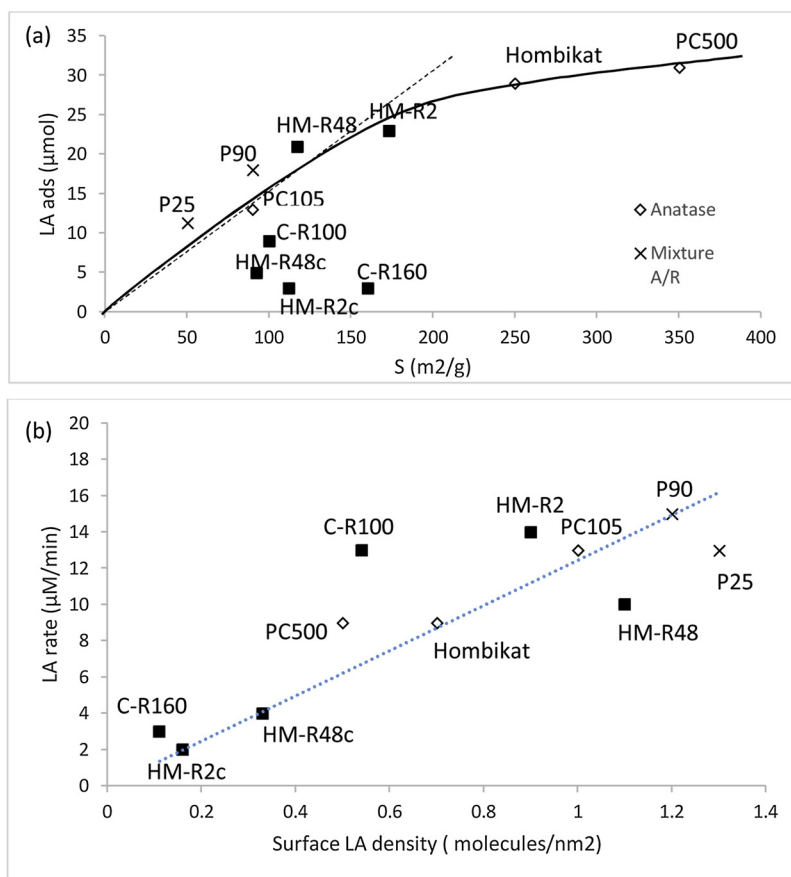
Fig. 4. (a) LA adsorption on the different TiO$_2$ samples as a function of the surface area, (b) Lactic acid disappearance rate as a function of the surface LA density.
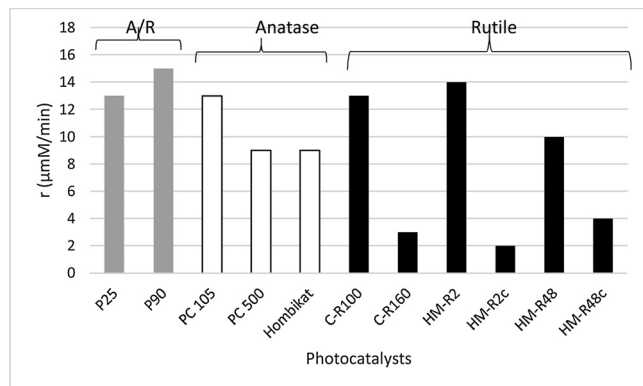

Fig. 5. Disappearance rate of lactic acid for the different TiO$_2$ samples. Grey histogram is for mixt anatase /rutile samples, white histogram for anatase samples and black histograms for rutile samples (For interpretation of the references to colour in this figure legend, the reader is referred to the web version of this article).

presence of iron.

Taking into account the correlation between LA disappearance rate and LA surface density, the literature values for the number of OH groups on TiO$_2$ Hombikat and TiO$_2$ P25, and the IEP values, the high reactivity of HM-R2 and HM-R48 could be explained by a sufficient amount of OH groups along with a high surface area. However, the low IEP values for non-calcined HM samples also show that the ionization state of the surface plays an important role. Several other groups also report successfully synthesizing high-efficiency pure rutile photo-catalysts [32–34]. These results challenge initial ideas about the efficiency of different phase compositions. The synthesis method for these

four samples used no organics, ensuring that any residual organic impurities from the synthesis process were limited. Moreover, TG-DTA-MS analysis confirmed the absence of residual chlorine and other impurities. Moreover, the surface areas obtained are substantial and the two highest performing samples are not calcined- allowing for the preservation of hydroxyl groups on the surface. These could be some of the reasons why HM-R2 and HM-R48 are so efficient relative to other commercial samples.

In summary, to have an efficient rutile phase photocatalyst it is necessary to limit the amount of surface impurities on the material. It is also important to have the maximum possible number of adsorption sites, mainly in the case of rutile where recombination of (e-, h+) pairs is notable due to the photocatalyst's direct band gap energy [7]. Therefore, it is necessary to avoid the use of organic precursor to prepare the photocatalyst. It is also important to synthesize the catalysts at a low temperature, avoiding the calcination step.

4.2. Photocatalytic degradation products of lactic acid in presence of anatase, rutile and anatase/rutile TiO$_2$ samples

Two main pathways can lead to the degradation of lactic acid under air: either dehydrogenation of alcohol into ketone to form pyruvic acid or decarboxylation to form ethanol. Both products are both transformed into acetaldehyde and finally into acetic acid as described into the Scheme 1. Acetic acid can be completely oxidized into CO$_2$ or can form methane and ethane in air as previously observed [35].

The formation of pyruvic acid and ethanol can be explained either by direct reaction with hole or by intermediate formation of OH° by oxidation of water with h$^+$.

Formation of ethanol was never observed in our case, regardless of the catalyst type. This is likely due to its lower formation and/or rapid
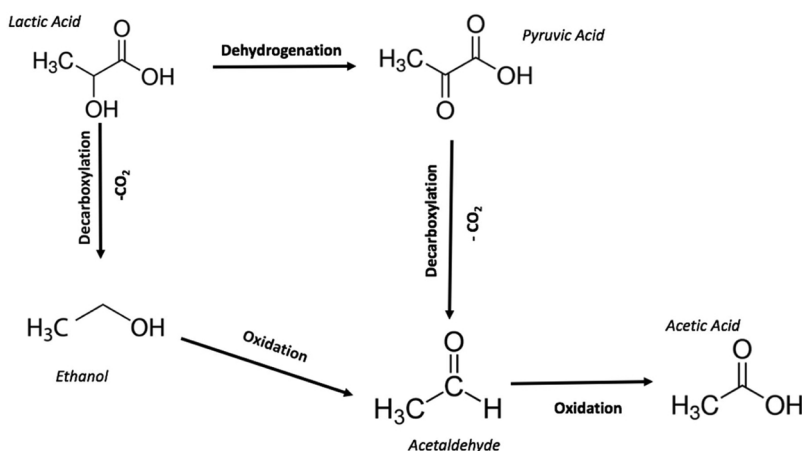
Scheme 1. Photocatalytic degradation of lactic acid in presence of photocatalysts.
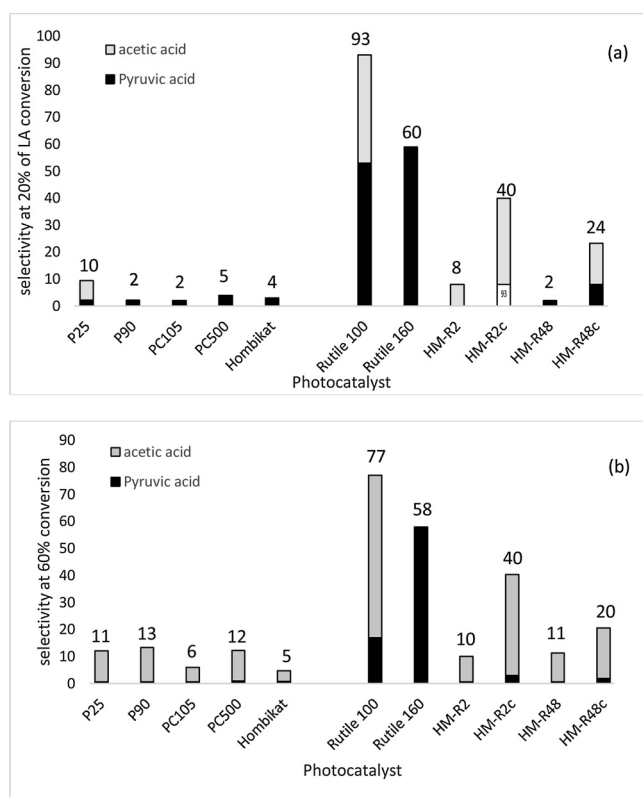
Fig. 6. Selectivity of pyruvic acid and acetic acid obtained at 20% (a) and 60% (b) of lactic acid conversion in presence of the different catalysts. The values given above each histogram correspond to the carbon balance determined taking into account acetic acid and pyruvic acid formation.

degradation. In fact, ethanol is a scavenger of OH° [36]. Only pyruvic acid and acetic acid have been observed in the aqueous phase. To better compare the difference in product formation between the samples of TiO$_2$, the percent selectivities of acetic acid and pyruvic acid were found. Percent selectivity determines what amount of a certain molecule is contained in the entire sample of degradation products at a certain time in the degradation process. The percent selectivities of pyruvic acid and acetic acid were identified at two points: when 20% and 60% of lactic acid had been converted (Fig. 6a, b). This helps determine the main composition of degradation products, and how they differ between photocatalysts. It seems that for all samples tested, as more lactic acid is converted, the amount of pyruvic acid decreases as acetic acid selectivity increases. These results suggest that the pyruvic

acid is directly transformed into acetic acid through decarboxylation.

The carbon balance is most nearly reached by commercial rutile C-R100 with a selectivity of 53% of pyruvic acid and 40% of acetic acid at a conversion of 20% of lactic acid. For all other catalysts, the carbon balances are low. They fall below 10% except for both home-made rutile catalysts calcined at 300 °C (HM-R2c and HM-R48c), which reach about 40% and 20% respectively.

With the exception of C-R160, all catalysts tested saw an increase in the selectivity of acetic acid accompanied by a decrease in selectivity of pyruvic acid- this was also observed by increasing the LA conversion, indicating the decarboxylation of pyruvic acid (Fig. 6).

We also observed that for all catalysts, acetic acid accumulates during the degradation process and a decrease in its concentration is never observed during the analysis period.

As observed in Fig. 6, the carbon balance is very low for most of the catalysts. Several hypotheses can be suggested to explain this behavior:

- formation of other intermediate degradation products
- intermediate formation of volatile organic compounds such as acetaldehyde
- high adsorption of pyruvic acid and acetic acid on the photocatalyst

Considering the first hypothesis, in literature dealing with the photocatalytic degradation of lactic acid [37,38], other compounds such as 2,3 butanediol or acetal could be formed coming respectively from direct photolysis of lactic acid and dehydrogenative coupling. However, these products have not been detected under our conditions.

Attempting to evaluate the formation of volatile compounds, we performed gas phase analysis for some of the catalysts. The gas phase products have been determined for four samples: a pure anatase phase (PC105), a mixed phase (P90), a pure rutile home-made sample (HM-R48), and the commercial rutile phase (C-R100) due to its good carbon balance. These catalysts have been chosen because of their similar surface areas. The detection of acetaldehyde and CO$_2$ is given in Fig. 7a and b.

The concentrations of these products do not correspond to the total initial amount of CO$_2$ or acetaldehyde formed because they are volatile and removed from the solution as a function of time. It is therefore not possible to give their selectivity. However, these results highlight that:

- Acetaldehyde is detected for all catalysts tested, except for C-R100 due to its rapid oxidation. This is in agreement with a total carbon balance observed, which is favored when iron is present on the surface of this catalyst. The rapid oxidation of acetaldehyde is also in agreement with the formation of an iron complex [39] and its reaction by photo-Fenton [40].
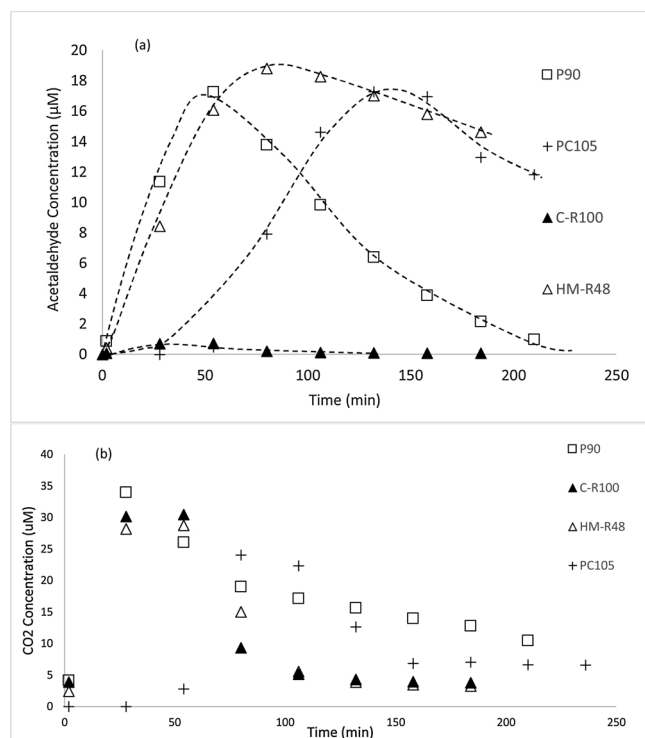- the concentration of acetaldehyde decreases after 50 min (P90),

Fig. 7. Formation of acetaldehyde (a) and CO_2 (b) as a function of irradiation time for a pure anatase phase (PC105), a mixt phase (P90), a pure rutile home-made prepared (HM-R48) and the commercial rutile phase (C-R100).

100 min (HM-R48) and 160 min (PC105), indicating a difference in oxidative reactivity towards acetaldehyde for each catalyst.

- During the first hours of photocatalytic degradation, the amount of CO_2 formed for P90 and HM-R48 are equivalent to the amount formed on C-R100. In contrast, the carbon balance is only reached for the latter catalyst, suggesting that pyruvic acid and/or acetic acid are probably adsorbed on the first two catalysts.

- In the presence of PC105, CO_2 and acetaldehyde are only detected after about 30 min of irradiation, whereas the LA disappearance rate is similar to those of P90 and HM-R48. This result could be explained by a rapid decomposition of lactic acid into pyruvic acid which may remain adsorbed on the surface of the catalyst.

The results of the analysis of CO_2 and acetaldehyde described above and the continuous formation of acetic acid observed as a function of time suggest that the low carbon balance obtained is probably due to a high adsorption of intermediate products on the surface of the catalysts. This hypothesis is in agreement with the important carbon balance observed for C-R160 and both home-prepared rutile calcined which has poor adsorption properties (Fig. 6).

The particular behavior of C-R100 (its significant disappearance rate and quasi total carbon balance) is explained considering the presence of iron on its surface. These conditions favor oxidation into acetic acid, which will be released into the aqueous solution due to poor adsorption capacity.

5. Conclusions

We successfully synthesized several rutile TiO_2 photocatalysts with high surface area (between 92 to 173 m^2/g) and with high photocatalytic efficiency. The rutile TiO_2 obtained after only 2 h of hydrolysis without calcination was the most highly performing photocatalyst. HMR-2 was more efficient than TiO_2 P25, a reference in the photocatalytic field. A longer hydrolysis time (48 h) is not beneficial and decreased the efficiency, but HMR-48 remains as efficient as TiO_2

PC500 and TiO_2 Hombikat. The calcination of these samples at 300 °C is harmful, leading to negligible efficiency.

Comparing the photocatalytic efficiency of our home-made TiO_2 with seven additional commercial TiO_2 samples allowed us to establish a correlation between photocatalytic efficiency and surface LA density. These results show the importance of the adsorption properties of TiO_2. They suggest that the low photocatalytic efficiency of rutile TiO_2, could be due to a low number of adsorption sites on rutile TiO2, something that is often found in literature when comparing rutile with anatase phase using model pollutants in pure water. This most likely corresponds to either the small amount of OH groups, or the ionization state of the surface area. It will be interesting to investigate whether these rutile samples with large specific surface areas always remain more active than anatase phase samples in the presence of different family of molecules- in particular, neutral compounds but also ones present in real wastewater. The analysis of organic intermediate compounds reveals the formation of both acetic acid and pyruvic acid for all TiO_2 samples tested. However, the carbon balance obtained by considering these two intermediate products is very low for all catalysts except for the two commercial rutile TiO_2 samples and, to a lesser extent, the calcined HM rutile samples. Considering the formation of acetaldehyde and CO_2 measured in gas phase and the continuous formation of acetic acid, the low carbon balance observed for the majority of the catalysts does not seem to be caused by higher mineralization. The significant detection of organic compounds in the aqueous phase at similar LA conversion for some catalysts seems to be linked to the lower adsorption site density.

A particular behavior was observed in both commercial rutile TiO_2 catalysts. They favor the formation of pyruvic acid. A pyruvic acid selectivity higher than 50% was found for these catalysts, indicating that decarboxylation is not the main pathway of LA degradation. Their high selectivity could be attributed to the presence of other inorganic compounds present on both commercial catalysts as revealed by XPS and ICP (Si in C-R160 and Fe, Al in C-R100). Further studies must be performed in order to better understand this behavior.

For all catalysts, except the two commercial samples containing inorganic impurities, only acetic acid was formed with high selectivity from the beginning of degradation, supporting the idea that the rapid decarboxylation of LA is due to the generation of OH radicals.

These results suggest that some commercial rutile TiO_2 samples appear to be particularly useful for selective photocatalytic oxidation of organic substrates, likely due to the presence of other atoms on the photocatalyst's surface.

Appendix A. Supplementary data

Supplementary material related to this article can be found, in the online version, at doi:https://doi.org/10.1016/j.apcatb.2019.04.042.

References

[1] M.N. Chong, B. Jin, C.W.K. Chow, C. Saint, Water Res. 44 (2010) 2997–3027.
[2] J.-M. Herrmann, C. Guillard, P. Pichat, Catal. Today 17 (1993) 7–20.
[3] C. Indermühle, E. Puzenat, F. Dappozze, F. Simonet, L. Lamaa, L. Peruchon, C. Brochier, C. Guillard, J. Photochem. Photobiol. Chem. 361 (2018) 67–75.
[4] Y. Paz, Appl. Catal. B. Environ. 99 (2010) 448–460.
[5] C. Colbeau-Justin, M. Kunst, D. Huguenin, J. Mater. Sci. 38 (2003) 2429–2437.
[6] J. Zhang, P. Zhou, J. Liu, J. Yu, Phys. Chem. Chem. Phys. 16 (2014) 20382–20386.
[7] T. Luttrell, S. Halpegamage, J. Tao, A. Kramer, E. Sutter, M. Batzill, Sci. Rep. 4 (2014) 4043, https://doi.org/10.1038/srep04043.
[8] T. Hirakawa, K. Yawata, Y. Nosaka, Appl. Catal. Gen. 325 (2007) 105–111.
[9] M. Qamar, M. Saquib, M. Muneer, Desalination 186 (2005) 255–271.
[10] J.M. Kesselman, G.A. Shreve, M.R. Hoffmann, N.S. Lewis, J. Phys. Chem. 98 (1994)

13385–13395.

[11] M. Buchalska, M. Kobielusz, A. Matuszek, M. Pacia, S. Wojtyła, W. Macyk, ACS Catal. 5 (2015) 7424–7431.
[12] S. Cong, Y. Xu, J. Phys. Chem. C 115 (2011) 21161–21168.
[13] Q. Sun, Y. Xu, J. Phys. Chem. C 114 (2010) 18911–18918.
[14] A.Y. Ahmed, T.A. Kandiel, T. Oekermann, D. Bahnemann, J. Phys. Chem. Lett. 2 (2011) 2461–2465.
[15] J.-M. Herrmann, Catal. Today 53 (1999) 115–129.
[16] M.R. Hoffmann, S.T. Martin, W. Choi, D.W. Bahnemann, Chem. Rev. 95 (1995) 69–96.
[17] P. Pichat, J.-M. Herrmann, C. Guillard, Catal. Today 17 (1993) 7–20.
[18] T. Ohno, T. Mitsui, M. Matsumura, J. Photochem. Photobiol. Chem. 160 (2003) 3–9.
[19] C.T. Bowmer, R.N. Hooftman, A.O. Hanstveit, P.W.M. Venderbosch, N. van der Hoeven, Chemosphere 37 (1998) 1317–1333.
[20] R.C. Loehr, Hazardous solid waste from agriculture, Environ. Health Perspect. 27 (1978) 261–273.
[21] R. Mueller, H.K. Kammler, K. Wegner, S.E. Pratsinis, Langmuir 19 (2003) 160–165.
[22] A. Di Paola, M. Bellardita, L. Palmisano, Z. Barbieriková, V. Brezová, J. Photochem. Photobiol. A: Chem. 273 (2014) 59–67.
[23] H.P. Boehm, M.Z. Herrmann, Z. Anorg, Allg. Chem. (1967) 352.
[24] R.-M. Mueller, H.K. Kammler, K. Wegner, S.E. Pratsinis, Langmuir 19 (2003) 160–165.
[25] P. Du, J.A. Moulijn, G. Mul, J. Catal. 238 (2006) 342–352.
[26] F. Batault, F. Thevenet, V. Hequet, C. Rillard, L. Le Coq, N. Locoge, Chem. Eng. J. 264 (2015) 197–210.
[27] T. Awatani, K.D. Dobson, A.J. McQuillan, B. Ohtani, K. Uosaki, Chem. Lett. 27

[28] (1998) 849–850.
[28] T. Ohno, K. Tokieda, S. Higashida, M. Matsumura, Appl. Catal. Gen. 244 (2003) 383–391.
[29] Q. Zhang, Appl. Catal. B Environ. 26 (2000) 207–215.
[30] Y. Nosaka, Y. Yamashita, H. Fukuyama, J. Phys. Chem. B 101 (1997) 5822–5827.
[31] J. Thiebaud, F. Thevenet, C. Fittschen, J. Phys. Chem. C 114 (2010) 3082–3088.
[32] J. Sun, L. Gao, Q. Zhang, J. Am. Ceram. Soc. 86 (2003) 1677–1682.
[33] M.S. Anwar, S. Kumar, F. Ahmed, N. Arshi, C.G. Lee, B.H. Koo, J. Nanosci. Nanotechnol. 12 (2012) 1555–1558.
[34] Y. Wang, L. Zhang, K. Deng, X. Chen, Z. Zou, J. Phys. Chem. C 111 (2007) 2709–2714.
[35] L.M. Betts, F. Dappozze, C. Guillard, Appl. Catal. Gen. 554 (2018) 35–43.
[36] D.E. Feierman, G.W. Winston, A.I. Cederbaum, Alcohol. Clin. Exp. Res. 9 (1985) 95–102.
[37] H. Harada, T. Sakata, T. Ueda, J. Am. Chem. Soc. 107 (1985) 1773–1774.
[38] K. Liu, A. Litke, Y. Su, B.G. van Campenhout, E.A. Pidko, E.J.M. Hensen, Chem. Commun. 52 (2016) 11634–11637.
[39] O. Khalipova, S. Kuznetsova, V. Kozik, AIP Conference Proceedings 1772 (2016) 020007, , https://doi.org/10.1063/1.4964529).
[40] M. Tokumura, A. Mizukoshi, M. Noguchi, Y. Wada, Y. Usami, T.Y. Yamaki, AIMS Environ. Sci. 3 (2016) 159–167.
[41] D. Gumy, C. Morais, P. Bowen, C. Pulgarin, S. Giraldo, R. Hajdu, J. Kiwi, Appl. Catal. B 63 (2006) 76–84.
[42] K. Doudrick, O. Monzón, A. Mangonon, K. Hristovski, P. Westerhoff, J. Environ. Eng. 138 (2012) 852–861.